Additive Manufacturing xxx (xxxx) xxx

Contents lists available at ScienceDirect

Additive Manufacturing

journal homepage: www.elsevier.com/locate/addma

Research Paper

Influence of residual stress and fluid–structure interaction on the impact behavior of fused filament fabrication components

Sumair Sunny, Huiluo Chen, Arif Malik *, Hongbing Lu

Department of Mechanical Engineering, The University of Texas at Dallas, Richardson, TX 75080, USA

ARTICLE INFO

Keywords:
Fused filament fabrication
Material extrusion
Fluid–structure interaction
Residual stress
Dynamic impact
Numerical modeling

ABSTRACT

Despite the proliferation of cellular fused filament fabrication (FFF) polymer components for a variety of industrial applications, few studies have investigated their fluid–structure interaction (FSI) behavior during loading, particularly under dynamic impact conditions. Furthermore, the extent to which residual stresses from the FFF build process affect the dynamic load bearing characteristics has not been addressed. In this work, simulations and experiments are conducted for cylindrical nylon specimens fabricated with two different internal closed-cell cavity structures to assess the influence of the entrapped fluid and the FFF residual stresses on the state of stress during high strain-rate impact. The demonstrated 2-stage computational approach includes a thermomechanical model of the FFF build to calculate residual stress and distortion, which forms the initial state for a subsequently executed dynamic impact model using smoothed particle hydrodynamics (SPH) to capture the effects of air within the internal cavities. Dynamic displacement boundary conditions for the FSI simulations are identified using digital image correlation (DIC), obtained from impact experiments on the FFF specimens performed using split Hopkinson pressure bar (SHPB) tests. Findings reveal that FFF residual stresses significantly influence the stress–strain response during dynamic impact, even at strain rates of 500–600 s^{-1}. In addition, while the influences of both FFF residual stress and FSI vary with internal cellular structure, the study reveals that their coupled effects must be considered to accurately characterize the impact behavior. Validity of the 2-stage numerical approach, as well as significance of FFF residual stress and the influence of FSI, are justified by comparing numerical predictions with experimental measurements, and observing root-mean-square stress errors within 12.77% and 11.87%, and peak stress errors within 1.93% and 1.34% for the two specimens.

1. Introduction

In contrast to dense, load-bearing engineered structures, those occurring in nature tend to be cellular, including, for example, bone, wood and coral [1]. Cellular structures may exhibit regular or irregular porosities, which can be considered as small cavities in the material matrix. Such structures are lightweight, stiff, and usually have higher specific strengths and higher specific impact energy absorption than their skeletal materials. Aside from foams, relatively few structures produced using traditional, large-scale manufacturing processes have exploited cellular or porous structural designs [2]. Additive manufacturing (AM) techniques, however, such as the fused filament fabrication (FFF) addressed in this work, readily accommodate nature-inspired creativity and allow for customized cellular structural designs that can result in superior functional performance, even with traditional engineering materials such as thermoplastics. A well-known issue in the additive manufacturing of both polymers and metals is development of residual stress and their associated geometric distortions, arising from non-uniform temperature distributions that vary with print pattern [3,4]. The prediction of residual stress and distortion in FFF, however, as well as their influence on the final part performance, requires a modeling approach different from those for conventionally manufactured components. This is due to the unique build process as well as the interactional effects of fluid (e.g. air) within closed-cell cavities of the printed structures during loading, whether the application involved is quasi-static or dynamic. Accordingly, without suitable predictive capability for the static or dynamic structural response of FFF parts, their application will remain limited to those allowing for significant trial-and-error. While the mechanical behavior and loading response of FFF polymer components have been previously investigated, they have either been mostly experimental or they neglect the coupled modeling of fluid–structure interaction and residual stress effects during dynamic

* Corresponding author.
E-mail address: Arif.Malik@utdallas.edu (A. Malik).

https://doi.org/10.1016/j.addma.2020.101662
Received 21 June 2020; Received in revised form 18 September 2020; Accepted 8 October 2020
Available online 14 October 2020

loading. For example, anisotropy in mechanical behavior, as governed by the print pattern, raster angle, filament diameter, etc., has been well documented [5–10]. Additionally, influence of the meso-structure (cellular infill pattern and infill density) on the macro-scale or bulk mechanical properties has been experimentally linked to the presence of FFF-induced porosities between longitudinally adjacent filament beads; such porosities vary as a function of width, thickness, and overlap of consecutive filament beads [11,12], as well as thermal and viscous behavior above glass transition. SEM micrographs of the fracture surfaces of FFF parts have confirmed the presence of these voids between adjacent beads of extruded filament [13]. Guessasma et al. incorporated X-ray micro-computed tomography to acquire 3D images of the voids formed during FFF [14]. They extended this approach to investigate how damage in terms of crack growth and inter-filament debonding propagates within a FFF specimen during uniaxial compression [15]. Their findings also highlight the importance of creating simulations based on the 3D image of a printed part, whose geometry might differ significantly from the idealized solid model. Note that the aforementioned inter-filament voids are not generally designed with intent since they are merely consequential to the FFF technique. In contrast, cellular cavities can be viewed as large-scale material voids that are designed with intent and comprise a regular infill pattern and density in FFF, usually to eliminate redundant material while maintaining functionality. Only a few studies on the macro strengths of polymer structures have been made that account for fluid within these cellular cavities. Mills et al. conducted finite element method (FEM) based impact simulations of low-density polyethylene (LDPE) and expanded polystyrene (EPS) foams with air-filled cavities, demonstrating favorable comparisons to experimental observations [16]. Their work, however, did not consider any effects of residual stresses on mechanical response. Sunny et al. incorporated FSI to model the effects of entrapped air within the closed-cell cavities of FFF nylon prints during quasi-static compression [17]. Their simulations predicted the residual stress, distortion, and temperature fields during FFF builds, followed by quasi-static compression predictions using various fluid–structure interaction techniques. The predicted macro compressive strengths were validated experimentally, and elucidate the importance of coupling the fluid–structure response. The aim of this work is to investigate the importance of incorporating FFF residual stress and FSI when predicting the state of stress in cellular nylon specimens subjected to dynamic impact. The technical approach involves a 2-stage numerical simulation: (1) Thermomechanical modeling of the FFF build to compute residual stress and distortion, and (2) Strain-rate sensitive dynamic impact modeling using smoothed particle hydrodynamics (SPH) to capture the FSI effects of air within the closed-cell cavities. The accompanying experimental work involves a setup similar to that described by Fila et al. and Ouellet et al. [18,19], and includes split Hopkinson pressure bar tests on the printed specimens as well as digital image correlation [20–23]. The high frame-rate images obtained by DIC are used to establish dynamic displacement boundary conditions for modeling the impact tests. Results of the model predictions, with and without inclusion of the FFF residual stress and the FSI, are compared with the experimental results to assess their isolated and coupled effects. Motivation for this work stems from the modeling and knowledge needed to design FFF polymer components for such applications as lightweight impact attenuators.

An overview of the 2-stage numerical modeling process is seen in Fig. 1. The sections that follow outline the 2-stage numerical modeling, FFF specimen fabrication, dynamic impact experiments, and discussion of the effects of FFF residual stress and FSI on the dynamic stress–strain response for two cylindrical nylon components having different cellular cavity structures, seen in Fig. 2.

2. Numerical modeling

Dynamic impact of non-AM cellular structures has been modeled in the past, but with simplifications. For instance, Karagiozova et al. modeled honeycomb structures of aluminum alloys 5052 and 5056 to study energy absorption but the elastic/perfectly-plastic material constitutive model neglected strain hardening effects during impact. Their work also did not consider any FSI effects between the air and aluminum, and thus assumed the prismatic honeycomb cells remained open at their ends during simulated impact [24]. Zheng et al. modeled the impact of a 3D Voronoi metal foam, and similarly neglected FSI effects [25]. Neither of the above included experimental validation. The only prior work involving FSI effects in AM cellular structures is that of Sunny et al., who studied the quasi-static compression of FFF nylon cuboids, finding that both coupled Eulerian–Lagrangian (CEL) and SPH type FSI methods were comparable in accuracy against benchmarked experiments, with SPH being more convenient to model. The modeling work here extends their steady-state approach to consider dynamic impact with FSI as a post-process to the FFF build. Rate dependency in the plastic constitutive model is considered to accommodate high strain-rate impact for the nylon specimens [26].

2.1. Stage 1: Thermomechanical FFF simulations

Thermomechanical simulation of the FFF build (denoted Φ1) involves a one-way coupled, 3D transient temperature-displacement Lagrangian finite element (FE) approach. Governing equations, assumptions, moving boundary conditions, and element activation technique to model the build are provided in this section following a brief review of related works. Brenken et al. [27] developed a physics-based extrusion deposition additive manufacturing (EDAM) process simulation tool for fiber-reinforced thermoplastic composites. The tool facilitated layer-by-layer material deposition that results in highly anisotropic layer properties. While their study focused on the material behavior of 50 wt% carbon fiber reinforced Polyphenylene sulfide, the method was found to be extendable to other polymer additive process simulations as well. A three-dimensional heat transfer analysis provided the thermal history of the deposition process to consider crystallization and transition from viscous fluid to a viscoelastic solid. Convection and radiation conditions were experimentally calibrated and applied to external surfaces of the part during printing. The mechanical modeling included crystallization kinetics [28] as well as thermoviscoelasticity [29]. Validation was based on comparison of the numerically predicted deformation to that observed experimentally, with less than 7% difference observed. Cattenone et al. [30] presented a framework for FFF process simulation that employed GCODE from the 3D printer to control the element activation sequence. A decoupled thermal and mechanical analysis was used. First, the heat conduction equation was solved, thereby generating thermal history for the build. Subsequently, the thermal history was used as a forcing function in a mechanical analysis to obtain distortion and residual stress. This approach is similar to that described by Ref. 31. The mechanical modeling used includes a thermal-elastic-plastic relationship. Model assessment was again done by comparison of the experimentally observed and numerically predicted part distortion. Errors at different locations of the part ranged from as high as 66.5% to as low as 1.3%. The thermomechanical FFF analysis framework for the study in this paper, which is presented in the following sections, shares similarities with the work of Refs. 27 and 30. As was done in [27], the thermal model is first experimentally calibrated (see Fig. 1), so as to attain the correct convective heat loss during the FFF process. Whilst the crystallization kinetics modeling technique by Ref. 27 provides for multi-scale insights, a simpler mechanical modeling approach similar to the works of Ref. 30 is adopted in this initial study of dynamic impact to reduce computational expense, whilst striving for reasonably accurate distortion and residual stress trends in the built part.

2.1.1. Thermal modeling during FFF printing

The thermal modeling approach employed for this work has also been presented in the works of several researchers. D'Amico and

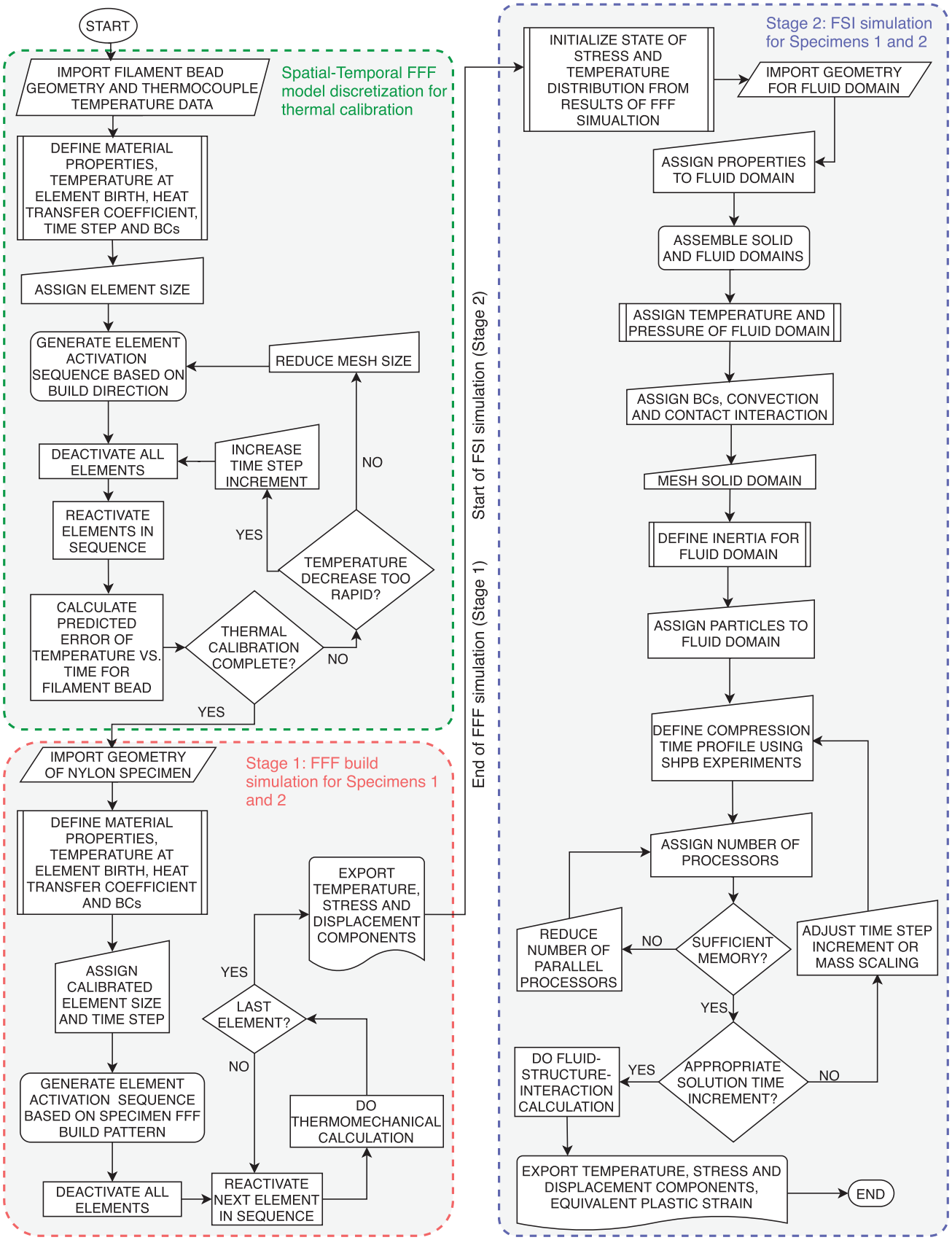

Fig. 1. Overview of the 2-stage numerical modeling process (with initial thermal calibration of extruded filament bead also shown).

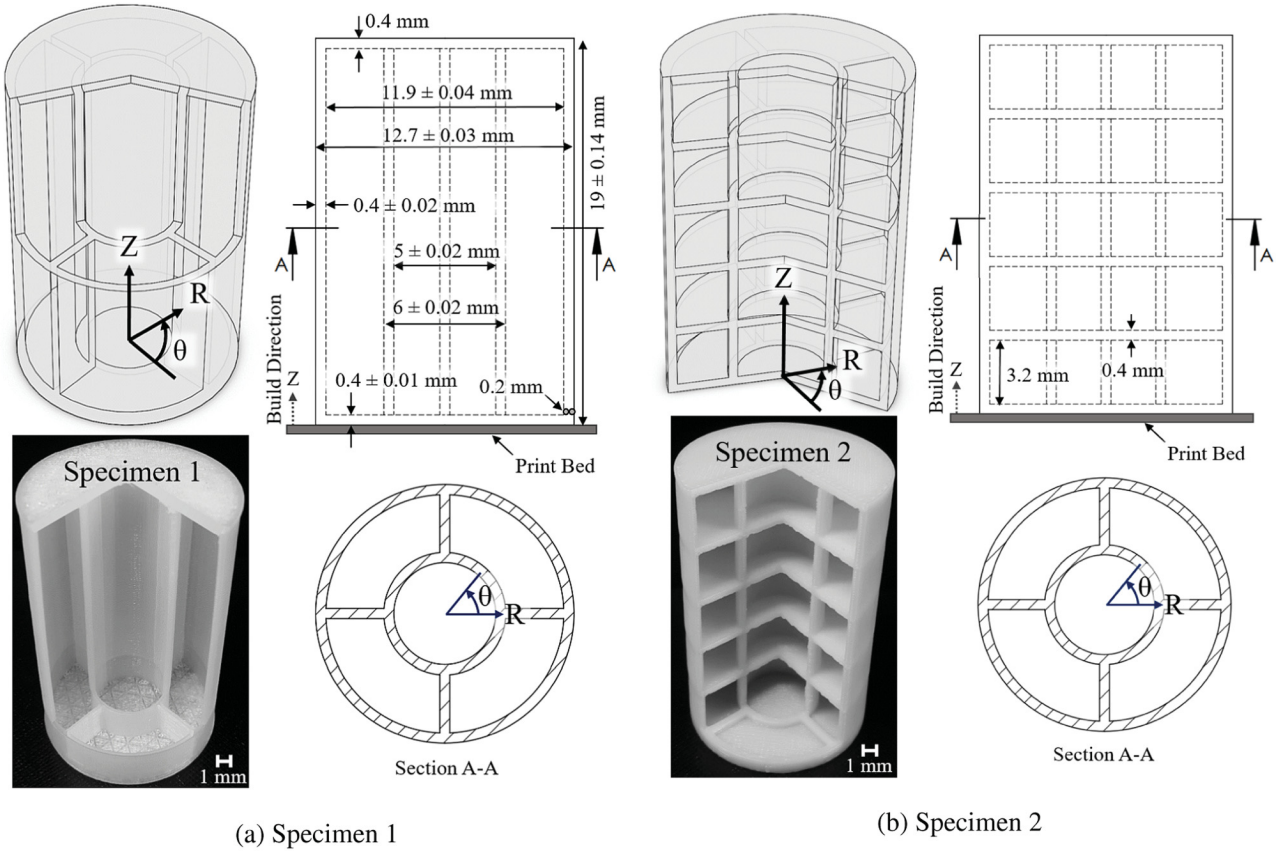

(a) Specimen 1 (b) Specimen 2

Fig. 2. Geometry and sample nylon FFF prints (with cut-away) revealing the closed-cell cavity structures. (a) Specimen 1. (b) Specimen 2.

Peterson [32,33] focused on numerical modeling to simulate the heat transfer to accurately capture the rapid cooling profile of extruded Acrylonitrile butadiene styrene (ABS) filament. Roy et al. [34] investigated the effects of material feed rate on the thermal history. They used infrared (IR) sensing during FFF using ABS to monitor the thermal profile; they then developed a transient FE model to investigate the influence of material feed rate on thermal history. This approach is not limited to FFF, and has also been used in various types of powder bed fusion (PBF) models [35–41].

The governing equation for the transient thermal analysis during FFF printing is:

$$q_v(t) - \rho_n c_{p_n} \frac{\partial T}{\partial t} + \nabla \cdot (-\boldsymbol{q}) = 0, \qquad \text{for} \quad t_{\Phi 1} > 0 \tag{1}$$

where q_v is the volumetric heat source in the solid (nylon) domain, t is time, ρ_n is mass density, c_{p_n} is specific heat, and T is temperature. Equation (1) is nonlinear due to temperature-dependent specific heat, c_{p_n}, and bulk thermal conductivity, k_n, the latter being in the heat flux vector, $\boldsymbol{q}$, defined in Eq. (2) [42,43].

$$\boldsymbol{q} = -k_n \nabla T \tag{2}$$

Initial conditions for the FFF build are given in Eq. (3), where T_0 is the initial temperature (459 K) of the j^{th} activated element (representing an extruded ‡hot‡ nylon filament segment) at activation time $t_{0,j}$, in accordance with the ‡inactive elements‡ approach to material extrusion discussed later in Section 2.1.3.

$$T(t_{0,j}) = T_0, \quad \text{for} \quad t_{\Phi 1} = 0 \tag{3}$$

Boundary conditions (which neglect radiation) are given by Eq. (4), where q_{conv} is the convective heat loss rate per unit area of all exposed element surfaces, S_i, at any time during FFF printing. T_∞ is ambient temperature (296 K), and h is the surface convective heat transfer coefficient defined in Eq. (5), as described in Ref. 44 wherein h_{free} represents the heat transfer coefficient of natural convection, and h_{forced} is that of forced convection.

$$q_{conv} = h(T - T_\infty) \quad \text{on} \quad S_i, \quad \text{for} \quad t_{\Phi 1} > 0 \tag{4}$$

$$h = h_{free} + h_{forced} \tag{5}$$

Given the minimal air movement within the enclosed MarkForged Mark 2 FFF printer used to build the nylon specimens, only h_{free} requires consideration, and is calculated using Eqs. (6) to (10) with d_f as the extruded filament diameter. Note that d_f also corresponds to the approximate size, L, of each ‡activated‡ finite element when simulating the print. In Eqs. (6) to (10), Nu, Ra, Gr, and Pr are the Nusselt, Rayleigh, Grashof, and Prandtl numbers, respectively. Terms μ and $\hat{\nu}$ are dynamic and kinematic viscosities, g is the gravitational constant, α and k_{air} are thermal expansion coefficient and thermal conductivity of air, respectively.

$$h_{free} = \mathrm{Nu}\ \frac{k_{air}}{d_f} \tag{6}$$

For laminar flow, $\mathrm{Ra} < 10^9$ [45]:

$$\mathrm{Nu} = 0.68 + \frac{(0.67\ \mathrm{Ra}^{\frac{1}{4}})}{\left[1 + \left(\frac{0.492}{\mathrm{Pr}}\right)^{\frac{9}{16}}\right]^{\frac{4}{9}}} \tag{7}$$

$$\mathrm{Ra} = \mathrm{Gr}\ \mathrm{Pr} \tag{8}$$

$$\mathrm{Gr} = \frac{g\alpha(T - T_\infty)L^3}{\hat{\nu}^2} \tag{9}$$

$$\mathrm{Pr} = \frac{c_p \mu}{k_{air}} \tag{10}$$

Temperature dependent thermal properties used for air are given in Ref. 17. Upon activation (extrusion) of each finite element-modeled nylon filament segment, the convective boundary conditions on its free surfaces S_i contribute to heat loss until ambient temperature is achieved. Similar to the approach of Ref. 27, the convection boundary condition used herein has been experimentally calibrated as described in Fig. 1 using a K-type contact thermocouple (accuracy ± 1.5% or ± 2 °C, whichever is greater).

2.1.2. Mechanical modeling during FFF printing

As noted earlier, to aid solution efficiency of the mechanical (displacement) behavior, an assumption is made to neglect body loads and inertial effects when simulating the FFF build. This implies that the extruded nylon filament solidifies sufficiently quickly such that viscous and gravitational deformations are small compared to the thermally induced deformations. Hence, equations of motion during the build are not needed, and the quasi-static stress equilibrium relation given in Eq. (11) governs structural behavior, where $\boldsymbol{\sigma}$ is the Cauchy stress tensor [46].

$$\nabla \cdot \boldsymbol{\sigma} = 0 \tag{11}$$

The thermal-elastic-plastic relationships in Eqs. (12) and (13) describe the extruded filament's constitutive behavior [30,47]. The mechanical modeling approach presented herein is not limited to FFF and has also been used for various powder bed fusion (PBF) simulations [35,40,41].

$$\boldsymbol{\sigma} = C(\boldsymbol{\varepsilon}_E) \tag{12}$$

$$\boldsymbol{\varepsilon}_E = \boldsymbol{\varepsilon} - \boldsymbol{\varepsilon}_P - \boldsymbol{\varepsilon}_{Th} \tag{13}$$

In Eq. (12), C represents the elastic constants for the nylon filament [48], which is considered homogeneous and isotropic but with significant temperature dependency, as detailed in Ref. 17. In Eq. (13), $\boldsymbol{\varepsilon}$ is the total strain tensor, and $\boldsymbol{\varepsilon}_E$, $\boldsymbol{\varepsilon}_P$, and $\boldsymbol{\varepsilon}_{Th}$ are the elastic, plastic, and thermal strain tensors, respectively. During printing, however, $\boldsymbol{\varepsilon}_P$ is absent due to the assumption of no inertial or viscous effects with the instantaneous and successive element activation (i.e. solidification) approach used (discussed in next section), and because thermal strains are insufficient to plastically deform the nylon during printing. Xia et al. [49] devised a computational model to understand how viscoelastic effects within the hot filament being extruded in FFF influences the shape and distribution of the rapidly solidifying filament bead. Their model predicted swell ratios at Reynolds number (Re) $= 1$ and Weissenberg numbers (Wi) ≤ 5 in good agreement with the work of Refs. [50,51]. Whilst the influence of viscoelastic consideration in the model was observable, the overall shape of the extruded filament did not differ significantly. Furthermore, with the printing of subsequent layers on top, the difference in shape of the underlying filament beads (height or thickness, and width) resulting from the influence of viscoelasticity was significantly reduced. For example, immediately after extrusion the bottom layer's thickness and width differed by approximately 14.8% and 4.9%, respectively, but after deposition of two additional layers, the variation for thickness (of the bottom layer) was indistinguishable, and that for the width was approximately 1.5%. Viscoelasticity thus can be considered to depend on the size of the ┼activated┴ finite elements, L, and is therefore not considered in this study.

The thermal strain herein is determined by Eq. (14), where, α_n is the coefficient of linear thermal expansion,[1] and $\boldsymbol{I}$ is an identity matrix [52].

$$\boldsymbol{\varepsilon}_{Th} = \alpha_n \Delta T[\boldsymbol{I}] \tag{14}$$

Prescribed displacement on the boundary during the build is given in Eq. (15), where X_b represents the FFF part's base. Sliding contact between the first printed layer and the print bed assumes critical shear Coulomb friction (coef. $= 0.5$) to permit lateral thermal expansion.

$$U_Z(X_b, t) = 0, \qquad \text{for} \qquad t_{\Phi 1} > 0 \tag{15}$$

2.1.3. Material extrusion modeling during FFF printing

Since the primary aim of this work is to establish the extent to which FFF residual stress resulting from the build affects the FSI-coupled stress response during high strain-rate impact, a brief discussion is warranted regarding the material extrusion modeling. Two approaches have been adopted for ┼adding┴ material during FEM simulation of AM, namely the *inactive* and the *quiet elements* methods [35,40,42,53,54]. In the *inactive elements* method used in this work, all elements of the FE model assume an initial deactivated state, leaving only nodal locations and degree-of-freedom (DOF) information. Elements are then sequentially activated, corresponding in this case to the extrusion of hot nylon filament segments, at 459 K. In contrast, with the *quiet elements* method, all elements persist but they are assigned negligible material property contributions until they are needed. With a highly refined mesh and significant material addition, the *quiet elements* method can be very computationally expensive. In the *inactive elements* approach used here, physical computing memory is reduced, but the method requires repeated equation numbering as new elements are activated. As determined by the thermal calibration procedure indicated in Fig. 1 a mesh size of 0.5 mm is used for the coupled temperature-displacement elements featuring reduced integration, along with a time step of 1 s

The thermomechanical modeling described above is performed to simulate residual stress in the FFF builds of the two nylon cylindrical structures having different internal closed-cell cavity configurations, as shown in Fig. 2a and b, respectively. Moreover, while the actual printed structures used for SHPB impact testing are built using a "circumferential" FFF print pattern, for the purposes of residual stress comparison only, both circumferential and rectilinear patterns are simulated (Fig. 3a and b).

Note that for each layer of the rectilinear pattern of Fig. 3a, the print priority is the Y direction, then the X direction. Successive layers correspond to increments in height Z. During simulation of the build, layer thickness corresponds to the filament diameter since gravitational and viscous effects of extruded filaments are neglected. For each layer of the circumferential print pattern of Fig. 3b, priority is set to circumferential (tangential) position, followed by radial position (largest to smallest), such that successive concentric rings, decreasing in diameter, are printed. Sequencing algorithms for simulation of the print patterns are coded in-house. An alternative to in-house sequencing algorithms is direct use of the printer's GCODE, but this was not available from the

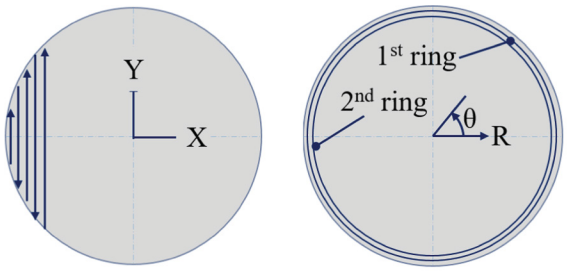

(a) Rectilinear Print Pattern. (b) Circumferential Print Pattern.

Fig. 3. FFF print patterns shown for the base of the specimens. While patterns remain the same, interruptions will be introduced as cross-sections vary along the build direction. (a) Rectilinear Print Pattern. (b) Circumferential Print Pattern.

[1] In the present study, given the temperature range and the nylon filament material,αn is assumed linear; however, this may not be the case for other materials.

manufacturer for the 3D printer used. Note that each element activation emulates (in piecewise continuous manner) the extrusion rate of the Mark 2 printer, and involves complete solution of an implicit, transient, coupled temperature-displacement problem, solved via finite difference and FE methods. Successive element activations (solutions) inherit the thermomechanical state from the preceding solution as an initial condition. The sequential activation is programmed using Python script, and solutions are obtained using an Abaqus v6.14 solver. To incorporate the actual interior and exterior print geometries of the nylon specimens in Fig. 2a and b, five replicates are fabricated using the ┼half-print┬ method [17] in addition to complete specimens used in the high strain-rate impact testing detailed in Section 3.

2.1.4. Stage 2: Fluid Structure Interaction Simulations during high strain-rate impact

The requirement to consider FSI between the air and the internal closed-cell cavity surfaces is to capture the increase in structural stiffness that results from the corresponding increases in air pressure as cavity volumes decrease and change shape during dynamic impact. Several numerical techniques exist for FSI simulation. In this work, smoothed particle hydrodynamics (SPH) is applied to model the fluid medium response [53] during the FSI impact simulations (denoted Φ2) that follow the FFF build simulations (Φ1). Using SPH as opposed to a Lagrangian formulation mitigates mesh related errors due to excessive element distortion. In this work, the prevailing question is whether the high strain-rate FSI stress response is influenced by residual stress arising from the FFF print. The fluid modeling is described below, and is followed by discussion of the SHPB experiments conducted on the FFF parts at strain rates of 500–650 s^{-1}.

2.1.5. Equations for the fluid domain during impact, and use of smoothed particle hydrodynamics

In this study, air is presumed to be the only fluid present within the closed-cell cavities of the nylon prints. An ideal gas equation of state per Eqs. (16) to (19) is adopted to accommodate pressure changes:

$$p + p_\infty = \rho R(T_{air} - T_{abs}) \tag{16}$$

$$E_m = E_{m_0} + \int_{T_{air_i} - T_{abs}}^{T_{air} - T_{abs}} c_v(T)dT \tag{17}$$

$$R = \frac{\tilde{R}}{MW} \tag{18}$$

$$R = c_p - c_v \tag{19}$$

where p is the air pressure, p_∞ is ambient pressure (101.325 kPa), ρ is air density, T_{air} and T_{air_i} are the current and initial air temperatures, respectively, T_{abs} is absolute zero temperature, E_m is specific energy, c_v is specific heat of air at constant volume, c_p is specific heat of air at constant pressure, $\tilde{R}$ is the universal gas constant (8.31451 J mol^{-1} K^{-1}), MW is the molecular weight of air (28.9585 g mol^{-1}) [55], R is the specific gas constant for air (287 J kg^{-1} K^{-1}), and E_{m_0} is the initial specific energy (at the initial temperature), which can be calculated using Eq. (20).

$$E_{m_0} = \int_0^{T_{air_i} - T_0} c_v(T)dT \tag{20}$$

Initial conditions for the fluid domain are:

$$T(t_{\Phi 2} = 0) = T_\infty \tag{21}$$

$$\begin{pmatrix} \sigma_R \\ \sigma_\theta \\ \sigma_Z \end{pmatrix} = p_\infty \quad \text{on} \quad \begin{pmatrix} S_R \\ S_\theta \\ S_Z \end{pmatrix}, \quad \text{for} \quad t_{\Phi 2} = 0 \tag{22}$$

where S_R, S_θ, S_Z represent internal cellular cavity walls having surface normals in the R, θ, and Z direction, respectively.

Smoothed particle hydrodynamics (SPH) is based on converting an integral interpolation scheme to a summation interpolation scheme. In brief, an integral interpolant for a function $S(\mathbf{r})$, given by Eq. (23), is approximated by a summation interpolant as seen in Eq. (24), where m_b is the mass of the b^{th} particle having density ρ_b.

$$S(\mathbf{r}) = \int S(\mathbf{r}')W(\mathbf{r} - \mathbf{r}', h_s)d\mathbf{r}' \tag{23}$$

$$S(\mathbf{r}) \simeq \sum_b m_b \frac{S_b}{\rho_b} W(|\mathbf{r} - r_\mathbf{b}|, h_s) \tag{24}$$

For a given kernel smoothing length h_s, Eq. (25) sums over all particles b within a $2h_s$ radius of the interpolating kernel $W(\mathbf{r}, h_s)$ centered on position $\mathbf{r}$. Using the summation interpolation, density to be used in Eq. (16) (equation of state) is approximated by Eq. (25): For a given kernel smoothing length h_s, Eq. (25) sums over all particles b within a $2h_s$ radius of the interpolating kernel $W(\mathbf{r}, h_s)$ centered on position $\mathbf{r}$. Using the summation interpolation, density to be used in Eq. (16) (equation of state) is approximated by Eq. (25):

$$\rho(\mathbf{r}) \simeq \sum_b m_b W(|\mathbf{r} - r_\mathbf{b}|, h_s) \tag{25}$$

The motion for compressible Newtonian fluids governed by the Navier–Stokes equation is seen in Eq. (26)[56–58].

$$\rho\left(\frac{\partial \mathbf{u}}{\partial t} + \mathbf{u}\cdot\nabla\mathbf{u}\right) = -\nabla p + \nabla\cdot\left(\mu(\nabla\mathbf{u} + (\nabla\mathbf{u})^\top) - \frac{2}{3}\mu(\nabla\cdot\mathbf{u})\boldsymbol{I}\right) + \boldsymbol{B} \tag{26}$$

Equation (26) relates inertial forces (left), with pressure forces, viscous forces, and body forces (right). Gingold et al. neglected viscosity in Eq. (26) and hence determined an equation of motion for the j^{th} element of a fluid with a volume $\Delta\mathbf{v}_j$, center of mass $\mathbf{r}_j$ and density ρ_j, as seen in Eq. (27), [59]:

$$\rho_j \Delta\mathbf{v}_j \frac{d^2\mathbf{r}_j}{dt^2} = -\Delta\mathbf{v}_j \nabla p + \rho_j \Delta\mathbf{v}_j \boldsymbol{B}_j \tag{27}$$

where ∇p is the pressure gradient at $\mathbf{r}_j$, and $\boldsymbol{B}_j$ is the body force acting on the j^{th} element. Particles are generated by uniformly discretizing an auxiliary Lagrangian mesh. In brief, the j^{th} particle is generated from the j^{th} element. Uniform discretization ensures uniform mass distribution of the fluid domain. During Φ2, due to interaction with the nylon structure, particles undergo displacement as a result of the compression boundary condition imposed on the nylon structure, discussed later in Section 3.2. The resulting divergence and curl of velocity $\mathbf{v}$ for particle a is approximated as seen in Eqs. (28) and (29).

$$\rho_a(\nabla\cdot\mathbf{v})_a \simeq \sum_b (\mathbf{v}_a - \mathbf{v}_b)\cdot\nabla_a W(|\mathbf{r}_a - \mathbf{r}_b|, h_s) \tag{28}$$

$$\rho_a(\nabla\times\mathbf{v})_a \simeq \sum_b m_b(\mathbf{v}_a - \mathbf{v}_b)\times\nabla_a W(|\mathbf{r}_a - \mathbf{r}_b|, h_s) \tag{29}$$

The SPH continuity, momentum, and thermal energy equations for compressible fluids are Eqs. (30) to (32) respectively [60,61]. Here ∇_a is a gradient taken with respect to the coordinates of particle a.

$$\frac{d\rho_a}{dt} \simeq \sum_b m_b(\mathbf{v}_a - \mathbf{v}_b)\nabla_a W(|\mathbf{r}_a - \mathbf{r}_b|, h_s) \tag{30}$$

$$\frac{d\mathbf{v}_a}{dt} \simeq -\sum_b m_b\left(\frac{p_b}{{\rho_b}^2} + \frac{p_a}{{\rho_a}^2}\right)\nabla_a W(|\mathbf{r}_a - \mathbf{r}_b|, h_s) \tag{31}$$

$$\frac{dE_a}{dt} \simeq \frac{1}{2}\sum_b m_b\left(\frac{p_b}{{\rho_b}^2} + \frac{p_a}{{\rho_a}^2}\right)(\mathbf{v}_a - \mathbf{v}_b)\nabla_a W(|\mathbf{r}_a - \mathbf{r}_b|, h_s) \tag{32}$$

Time stepping schemes for SPH are discussed in detail in Ref. 62. The Euler predictor-corrector employed herein serves as an explicit scheme well suited to FSI simulations [60]. It compliments a time increment

control that considers Courant conditions, force terms along with viscous diffusion effects. Cubic kernels are used in this work although various kernels $W(\mathbf{r}, h_s)$ can be used for SPH [63]. The difference in kernel order, typically ranging from 2 to 5, pertains to the number of neighboring particles [61,64,65]. The order affects the accuracy, smoothness and computational efficiency, [66].

2.1.6. Mechanical equations for lagrangian (solid) domain during impact

At the end of the FFF build simulation, Eqs. (1), (2), (4), (11), (14), (15) for the Lagrangian domain remain in place for the impact simulation. The primary modification introduces strain rate dependency in the plastic constitutive behavior. Damage is not modeled and, as seen later in Section 3.2, fracture was not observed during experiments. Thus, Eqs. (12) and (13) are modified at every time increment (Δt), per Eqs. (33) to (36) where, ($\dot{\boldsymbol{\varepsilon}}_p$) is the equivalent plastic strain rate.

$$\Delta\boldsymbol{\varepsilon}_p = \dot{\boldsymbol{\varepsilon}}_p \Delta t \tag{33}$$

$$\Delta\boldsymbol{\varepsilon}_E = \Delta\boldsymbol{\varepsilon} - \Delta\boldsymbol{\varepsilon}_p \tag{34}$$

$$\Delta\boldsymbol{\sigma} = C(\Delta\boldsymbol{\varepsilon}_E) \tag{35}$$

$$\boldsymbol{\sigma}_{n+1} = \boldsymbol{\sigma}_n + \Delta\boldsymbol{\sigma} \tag{36}$$

To include the final state of residual stress from Φ1 as the initial state prior to dynamic impact loading, the initial conditions for Φ2 are:

$$T(t_{\Phi 2} = 0) = T_{f,\Phi 1} \tag{37}$$

$$\boldsymbol{\sigma}(t_{\Phi 2} = 0) = \boldsymbol{\sigma}_{f,\Phi 1} \tag{38}$$

where $T_{f,\Phi 1}$ and $\boldsymbol{\sigma}_{f,\Phi 1}$ are the final temperature and state of stress at the end of stage 1 (Φ1), i.e., upon completion of the print. For the thermal boundary conditions, note that the surface convection from Eq. (4) and the ambient temperature, T_∞, remain unchanged . The ideal gas equation is given in Eq. (39).

$$pV = n\widetilde{R}T \tag{39}$$

Here, V is volume and n is number of moles. Equation (39) reduces to Eq. (40), in which $\hat{k}$ is the proportionality constant assuming that no fluid escapes the cavities. Note that while the foregoing assumption ignores possible rupture, the experimental results introduced later support this assumption for the particular specimen configurations tested.

$$\Delta p = \hat{k}\Delta T \tag{40}$$

As described in Ref. 17, an extruded filament bead used for thermal model calibration cools to ambient temperature in about 120 s. Accordingly, all elements of the Lagrangian model could be allowed to cool naturally to room temperature prior to subsequent high strain-rate testing. However, in a time-dependent, explicit, coupled temperature-displacement solution where small time steps are required to satisfy relatively refined meshes, computation time can be long. Referring to the earlier Eq. (4) for the convective heat transfer rate, it is noted that the cooling time (and thus computation time) can be reduced significantly by artificially increasing the convective coefficient, h, while still realizing the same heterogeneous final pressure states within the cellular cavities. Considering Eq. (5), it can therefore be assumed that the printed nylon part is subjected to artificial forced convection; the associated heat transfer coefficient, h_{forced}, although not rigorously required, can be obtained from Eqs. (41) to (43), [67]:

$$h_{forced} = \mathrm{Nu}\ \frac{k_{air}}{L} \tag{41}$$

Assuming laminar flow (Re $<$ 500,000),

$$\mathrm{Nu} = 0.664\ \sqrt{Re}\sqrt[3]{Pr} \tag{42}$$

$$\mathrm{Re} = \frac{u_m L}{\hat{\nu}} \tag{43}$$

In Eq. (43), u_m is the mean velocity of the external cooling fluid (air), and L is the length across a Lagrangian element. Considering the length of the smallest element, L_{min}, the time step criterion, Δt, for the Lagrangian domain is given by:

$$\Delta t\left(\frac{c}{L_{min}}\right) \leq 1 \tag{44}$$

Solution for the transient, coupled SPH-FE problem is obtained explicitly using Abaqus v6.14. The simulated FSI impact is accomplished by rapid movement of rigid boundary plates representing the surfaces of the incident and transmission bars in the SHPB experiments depicted in Fig. 4. The dynamic boundary conditions of these simulated rigid plates are assigned in accordance with the SHPB compression test profiles discussed next.

3. Impact testing

3.1. Split Hopkinson pressure bar tests

A modified SHPB setup involving a pulse shaping technique, shown in Fig. 4, is used to conduct dynamic impact compression tests on the FFF nylon parts. The apparatus consists of a solid 304 L stainless steel incident bar (Young's modulus 196 GPa, density 8000 kg/m^3, bar wave speed 4950 m/s), a solid 7075-T6 aluminum bar (Young's modulus 71.7 GPa, density 2810 kg/m^3, bar wave speed 5051 m/s) and a strain data acquisition system. The incident and transmission bars have 19 mm diameter, and respective lengths of 8.7 m and 3.66 m. Brass 260 disk pulse shapers having 1.092 mm thickness and 12.7 mm diameter are applied at the impact end of the incident bar. A thin layer of Dow Corning high-vacuum grease is applied at the interface between the pulse shaper and the incident end of the steel bar. Each nylon FFF specimen is inserted in an axial configuration directly between two bar ends of the SHPB apparatus for the dynamic compression (held using the same vacuum grease). A 1.8 m long steel striker, with the same diameter as both the incident and transmission bars, is launched by compressed air in the gas gun (not shown in Fig. 4), so that it impacts the pulse shaper and generates a desired compressive wave traveling in the incident bar to induce a nearly constant strain rate in the nylon specimen. Trap momentum is used to apply a single loading. An HBM Genesis digital oscilloscope (15-bit resolution, 25 MS/s sampling rate) is used to acquire strain signals through Wheatstone bridges and a Vishay 2310B signal conditioning amplifier connected to the strain gages (amplifier gain 1–11,000 continuously varying; 180 kHz frequency response, 180 kHz bandwidth and ± 0.02% linearity). A preset gap (δ) of 15.875 mm is used. Images of the incident bar at 8000 frames per second (fps) are captured by a Photron Fastcam SA6. Given its 2.76 μs shutter speed, the camera enables calculation of velocity during impact, which, as described below, is subsequently used with digital image correlation (DIC) software [21,68] to assign boundary conditions for the impact simulations. A test pressure of about 100 kPa, from a compressed air tank, is used to deliver an incident bar travel velocity (v) of 13.89 m/s, based on the specimen dimensions and deformation magnitude observed through preliminary experimentation.

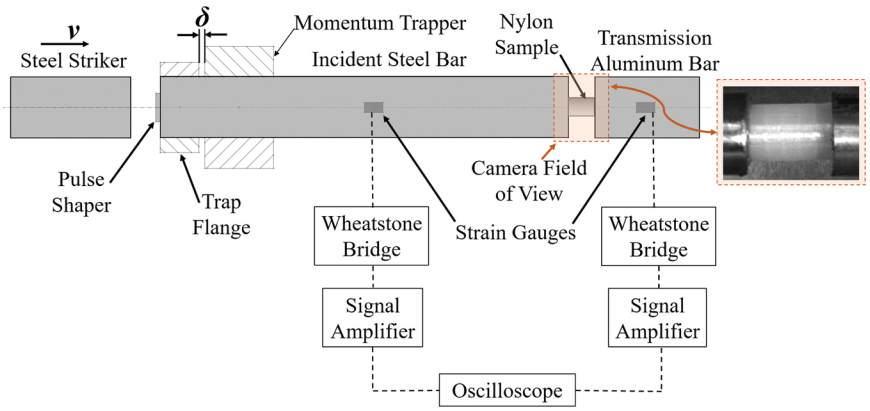

Fig. 4. Schematic of split Hopkinson pressure bar (SHPB) setup. A specimen is inserted such that Z axis is co-linear with the axes of the bars.

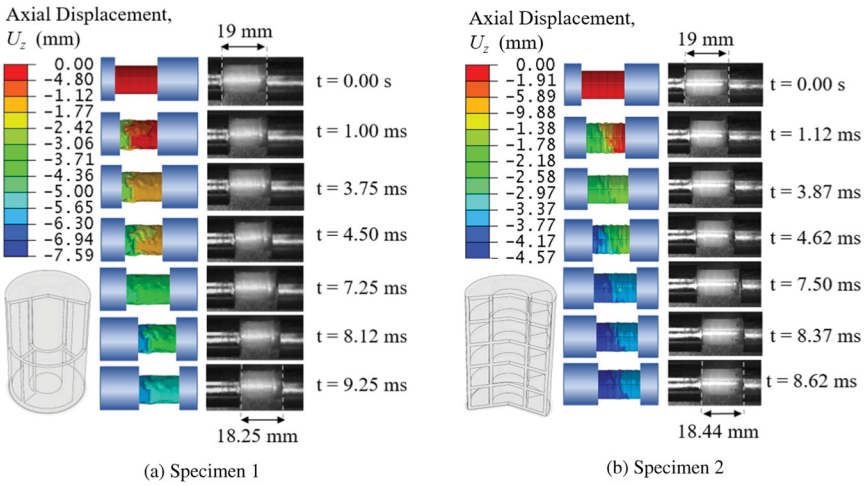

Fig. 5. Frames (grayscale) captured during high strain-rate experiments performed on SHPB, exhibiting deformation evolution for (a) Specimen 1 and (b) Specimen 2. Also pictured are corresponding FSI simulation images (color) for which displacement boundary conditions are established using DIC from the SHPB tests (the simulations are used in Section 4 for detailed analysis of the effects of FFF residual stress and FSI on the stress–strain response during impact). The simulated specimens feature FFF induced residual stress predicted in Stage 1. (a) Specimen 1. (b) Specimen 2.

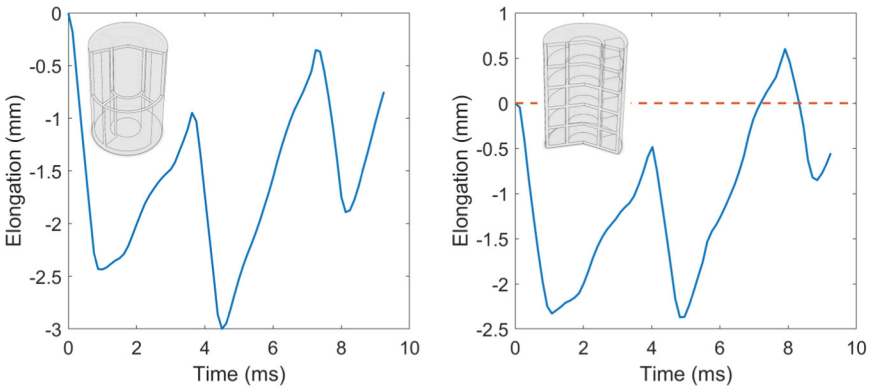

Fig. 6. Incremental compression and elastic recovery observed using DIC. (a) Specimen 1. (b) Specimen 2.

3.2. Digital image correlation (DIC) to determine impact simulation boundary conditions

As seen in Figs. 5 and 6, during SHPB testing with FFF Specimens 1 and 2, ┼incremental╌ motion in the incident bar is observed during impact, indicating intermittent elastic recovery between successive compressive increments. These rapid compression and elastic recovery cycles are subsequently used to assign nonlinear displacements (in time) for the rigid boundary plates in the impact simulations that are used to investigate the influences of FSI and FFF residual stresses on the dynamic stress response. Note that damage (fracture) was not observed to occur.

3.3. Experimentally derived strain-rate and stress–strain response

Equations (45) and (46) define the stress and strain rate profiles in a

specimen subject to dynamic impact using a SHPB [20].

$$\sigma_s(t) = \frac{A_t}{A_s} E_\tau \varepsilon_\tau(t) \tag{45}$$

$$\dot{\varepsilon}_s(t) = \frac{1}{\gamma_s}[(c_i - c_\tau \frac{E_i A_i}{E_\tau A_\tau})\varepsilon_i(t) - (c_i + c_\tau \frac{E_i A_i}{E_\tau A_\tau})\varepsilon_r(t)] \tag{46}$$

where subscripts i, τ and r represent incident, transmitted and reflected signals, respectively; E represents Young's modulus, A are cross-sectional areas at contact interfaces, c is the bar wave speed, γ is the length of the specimen, σ is the stress, and ε is the strain. Subscript s denotes the specimen. Equation (45) gives the stress history, and Eq. (46) provides the strain rate history, which, upon integrating in time, gives strain. Fig. 7a shows the experimentally determined compressive strain rate history from Eq. (46) during the initial impact wave for each specimen. Averages within the plateau regions of each curve indicate that Specimens 1 and 2 undergo, respectively, strain-rates of approximately 607 s^{-1} and 532 s^{-1}, with variations resulting from their different structural rigidities due to number and size of internal cellular cavities. Fig. 7b shows the experimentally acquired compressive axial stress–strain response of both specimens, per Eq. (45). Note that the stress–strain data is used for subsequent assessment of the computational models used to predict the residual stress induced by the FFF printing, as well as the FSI effects within the closed-cell cavities.

4. Results and discussion for numerical predictions

In similar fashion to the validation methodology presented by Refs. 27 and 30 for a thermomechanical FFF process simulation, a comparison of the simulated FFF build with the actual build is provided before subsequent detailed analysis into the effects of FFF residual stress and FSI. Accordingly, variations in the dimension parameters (L_1 to L_4), listed in Table 1, are evaluated. FFF simulated dimensions are compared only for the circumferential print pattern (Fig. 3b) as it more closely represents the proprietary pattern used by the Mark 2 printer when fabricating the physical specimens used for experimental measurement. Note that the relative difference for all parameters is less than 1%. It is observed that the actual printed specimen measurements are all slightly greater than the simulated values. Such slight differences may be the result of neglecting viscoelastic effects in the material model for nylon since any ⸢swelling⸣ phenomena as the viscoelastic polymer exits the extruder, as discussed by Xia et al. [49], are not considered. Fig. 8.

4.1. Numerically predicted influence of FFF print pattern on residual stress

Prior to evaluating the degree to which residual stresses from the FFF printing affect the subsequent state of stress during high rate impact, the peak compressive and tensile FFF residual stresses are first reported. Table 2 shows the computed peak component values for Specimen 1 (Fig. 2a) when printed with the rectilinear and circumferential print patterns shown earlier in Fig. 3a and b. Note that these peak stresses occur within the base layer.

Comparing the peak tensile and compressive stress components for both print patterns, as might be expected, the variation in axial stress σ_Z (in the build direction) is lower than for the radial stress (σ_R) and tangential (hoop) stress (σ_θ), both of which show considerably greater variation. Compressive radial stress for the rectilinear print pattern is

Table 1
Comparison of predicted and experimentally measured dimensions for the FFF builds of Specimens 1 and 2. Experimentally determined values obtained using Vernier caliper measurements for L_1 to L_4 as seen in Fig. 8.

Specimen	Parameter	Experimental measurement (mm)	Simulated value (mm)	Sim. error relative to expt. (%)
1	L_1	12.70	12.66	−0.31
	L_2	12.71	12.67	−0.31
	L_3	12.73	12.62	−0.86
	L_4	19.01	19.00	−0.05
2	L_1	12.71	12.67	−0.31
	L_2	12.74	12.62	−0.94
	L_3	12.72	12.65	−0.55
	L_4	19.12	19.00	−0.63

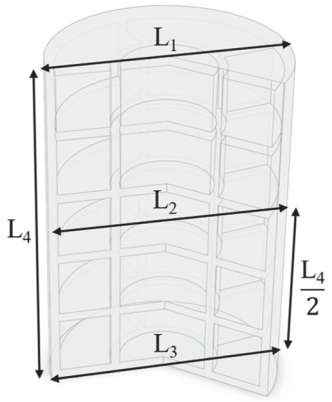

Fig. 8. Parameters (L_1 to L_4) for comparison between simulated and actual FFF builds (same for Specimens 1 and 2).

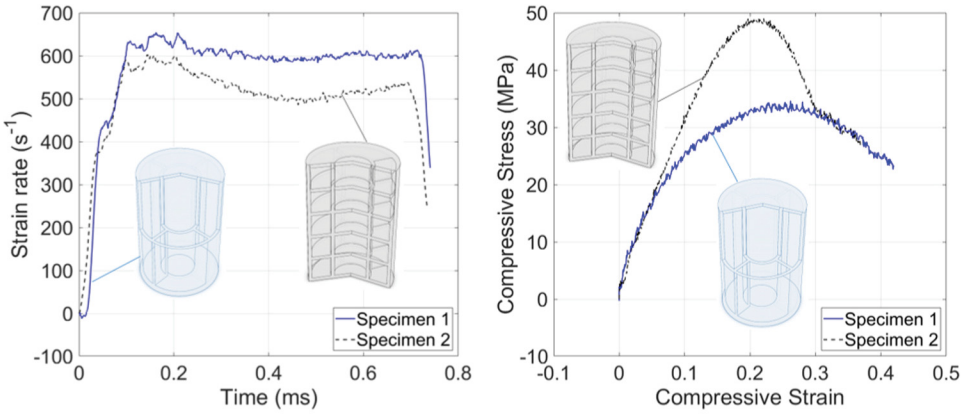

(a) Strain-rate (b) Stress-strain

Fig. 7. Experimental compressive axial responses for Specimens 1 and 2 during SHPB compression tests. (a) Strain-rate. (b) Stress–strain.

about 5 times that of the circumferential pattern. Compressive tangential stress for the circumferential pattern is approximately 2.8 times greater than that for the rectilinear pattern. These variations can be associated to the respective thermal histories within print layers. Depending on the print sequence, elements get activated such that they are still expanding when the adjacent elements are activated. Greater compressive radial stress is induced for the rectilinear pattern towards the end of the layer since the print path is shortened and elements are printed in close proximity over relatively shorter time. A similar explanation is given for the difference in tangential stress based on the print priority from the largest to the smallest concentric rings (Fig. 3b).

While the peak FFF residual stresses are mainly observed in the elements in base and ceiling layer(s), the different print patterns also play a significant role in terms of distortions that vary with build direction. This is observed in Fig. 9a, which shows distortion magnitude over the vertical (height) line (R, θ)= (4.42 mm, 3.23 rad). It is evident that distortion magnitude fluctuates more for the rectilinear print pattern along the build direction. Note, however, the peak distortion, observed at the conclusion of the build, is greater for the circumferential pattern; a peak distortion of 80.1 μm is observed with the circumferential print pattern at (R, θ, Z) = (6.35 mm, 2.47 rad, 0.5 mm), whereas a peak distortion of 51.4 μm is observed with the rectilinear print pattern at (R, θ, Z) = (3.27 mm, 1.91 rad, 18.5 mm). As with residual stress, this again relates to the respective thermal history, comparison for which is given in Fig. 9b at the specific point (R, θ, Z) = (6.35 mm, 3.14 rad, 9 mm). It is noteworthy that the more frequent local peaks in temperature observed with the circumferential pattern reduce fluctuation in the thermal distortion as a function of build height, but result in greater overall distortion. Two trends can be observed in Fig. 9b; first, the exponential drop in the temperature of the extruded filament, as it rapidly cools, is analogous to observations made by Seppala and Migler at NIST [69], who used IR measurements to obtain temperature profiles for extruded ABS polymer in order to comprehend the thermodynamic and kinetic states during a polymer bead's weld formation. Secondly, after the initial thermal spike subsides there are relatively smaller spikes that follow as the hot filament is extruded in close proximity to the probed location. This behavior is similar to that observed by Roy et al. [34].

Table 2
Peak tensile and compressive FFF residual stresses for circumferential and rectilinear print patterns (Specimen 1), occurring within the base of the specimen.

Peak stress components	Circumferential print pattern (MPa)	Rectilinear print pattern (MPa)
Tensile radial stress, $\sigma_{R,T}$	3.75	5.21
Compressive radial stress, $\sigma_{R,C}$	0.131	0.661
Tensile tangential stress, $\sigma_{\theta,T}$	7.16	8.45
Compressive tangential stress, $\sigma_{\theta,C}$	1.88	0.659
Tensile axial stress, $\sigma_{Z,T}$	7.22	4.92
Compressive axial stress, $\sigma_{Z,C}$	3.574	3.926

4.2. Influence of FFF residual stress and FSI on stress–strain response during high strain-rate impact

4.2.1. Comparison of experimental and numerically predicted axial compressive stress–strain response

The influences of FFF residual stress and FSI on the numerically predicted stress–strain response occurring during high strain-rate impact are now presented and discussed for both specimens. Recall from Fig. 2a and b that Specimen 1 has five internal fluid cavities spanning almost the full length, whereas Specimen 2 has twenty-five smaller cavities. FFF residual stress effects are examined only for the circumferential print pattern since it more closely represents the proprietary pattern used by the Mark 2 printer on which the SHPB test specimens were fabricated. Dynamic impact simulations for Specimens 1 and 2 are performed, using the computational approach outlined in Section 3, with and without including the FSI and FFF residual stress effects, respectively, as indicated in Table 3.

Inspection of Fig. 10a and b shows that inclusion of both FFF residual stress and FSI effects (as in Case 4 in Table 3) leads to better overall representation of the high-rate impact behaviors for both nylon specimens. Both the general trends and the values predicted for Case 4 (which includes FFF residual stress and FSI) are closer overall to the experimental results than for any other case in Table 3. However, due to differences in the number of cellular cavities, volume within cavities, and the different quantities of nylon printed with Specimens 1 and 2, the contributions of FFF residual stress and FSI not only vary for each

Table 3
Simulation cases used to investigate the influence of FSI and FFF residual stress during high strain-rate impact behavior for Specimens 1 and 2.

Simulation case	FFF residual stress	FSI
1	No	No
2	Yes	No
3	No	Yes
4	Yes	Yes

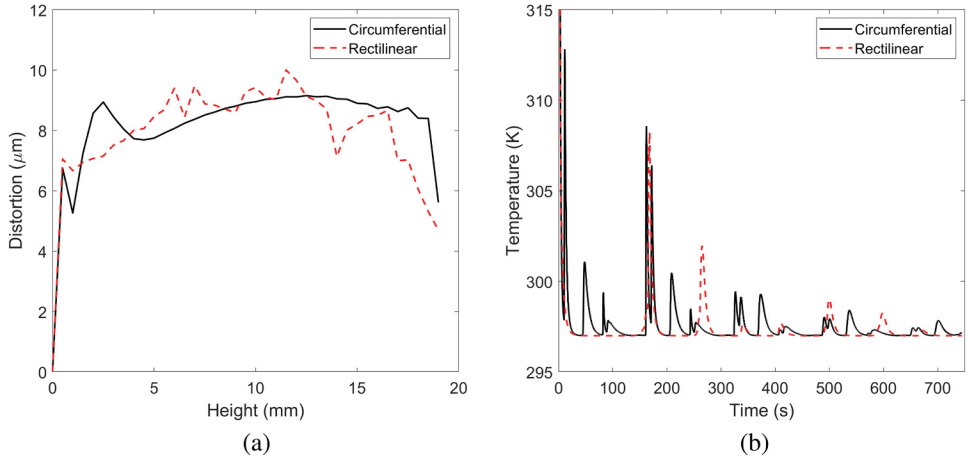

Fig. 9. Distortion and thermal history observed in Specimen 1 with different print patterns. (a) Distortion magnitude as a function of build height for circumferential and rectilinear FFF print patterns in Specimen 1 along vertical line (R,θ) = (4.42 mm, 3.23 rad). (b) Thermal history for both print patterns in Specimen 1 at location (R, θ, Z) = (6.35 mm, 3.14 rad, 9 mm). Note: data at 459 K for element ┼birth┼ during printing is omitted.

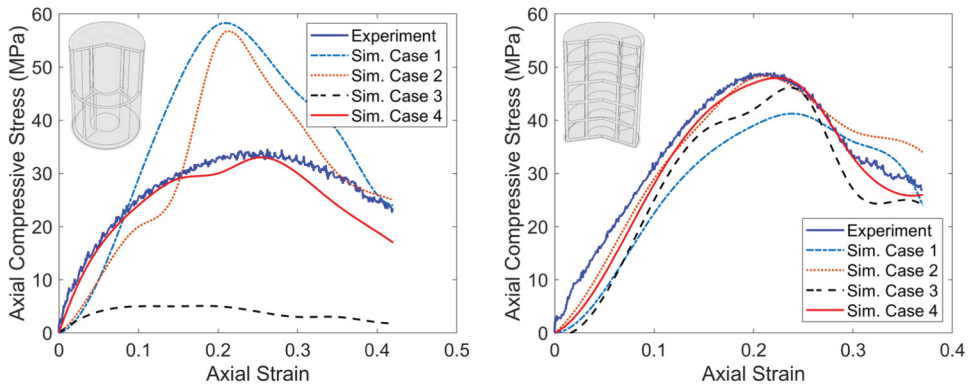

Fig. 10. Comparison of experimental and simulated compressive axial stress–strain response for both specimens. (a) Specimen 1. (b) Specimen 2.

Table 4
Comparison of root-mean-square (RMS) error between experimentally determined and simulated compressive axial stress–strain response, with and without considering effects of FFF residual stress and FSI in the numerical model.

Case number	Sim. vs. expt. compressive axial stress–strain response, $\sigma_{Z,C}$	Specimen 1	Specimen 2
1	RMS deviation (w/out FFF, w/out FSI)	13.14 MPa	6.41 MPa
	RMS relative error (w/out FFF, w/out FSI)	42.50%	22.99%
2	RMS deviation (with FFF, w/out FSI)	9.74 MPa	3.76 MPa
	RMS relative error (with FFF, w/out FSI)	31.62%	14.09%
3	RMS deviation (w/out FFF, with FSI)	23.44 MPa	5.76 MPa
	RMS relative error (w/out FFF, with FSI)	83.36%	26.29%
4	RMS deviation (with FFF, with FSI)	3.29 MPa	2.25 MPa
	RMS relative error (with FFF, with FSI)	12.77%	11.87%

specimen, but are also manifested differently in each one. Some specific observations and corresponding discussion follows. Table 4 indicates the overall accuracies of the numerically predicted stress–strain responses during impact. Shown are the root-mean-square (RMS) deviations (in MPa) and RMS errors (in %) relative to the experimentally observed stress–strain responses for both specimens.

Specimen 1:

- Refering to Fig. 10a, the results for Cases 1 and 2 clearly show that, without considering FSI, the predicted axial, compressive stress response during impact is significantly overpredicted compared to the experimentally measured stress for most values of the strain, including during the pre- and post-peak conditions. For Case 1, which does not consider the effects of FFF residual stress or FSI, the impact stress is drastically over-predicted for strain values from about 0.08–0.40, while the stress is slightly under-predicted from 0 to 0.08 strain. The peak predicted stress for Case 1 is almost double the experimentally measured value (58.46 MPa vs. 33.09 MPa). With the inclusion of FFF induced residual stress (but still no FSI) as in Case 2, the trend in the stress–strain response also reveals significant overprediction relative to the experimental stress beyond about 0.08 strain, except that the overpredicted stress is generally lower overall than when FFF residual stress is neglected in Case 1. Accordingly, the predicted stress–strain response for Case 2 is closer to the experimental response beyond strains of about 0.32. Interestingly, a momentary decrease in the gradient of the predicted stress–strain response for Case 2 occurs around 0.12 strain; this is due to early localized material yielding as a result of including the residual stress but not the FSI, since the main effect of FSI is to mitigate localization of stress through redistribution of the load burden to much more of the structure.
- When FSI effects are included, the absence of FFF induced residual stress leads to significant under-prediction of the compressive stress–strain response during impact. Therefore, in Case 3, which neglects FFF residual stress but includes FSI, value of the predicted stress peak is 4.01 MPa, which is far lower than the 33.09 MPa experimentally determined peak axial compressive stress.
- When both the FSI and FFF residual stress effects are included, as in Case 4, the predicted stress–strain response during impact is clearly much closer to the experimental values over a majority of strain values, particularly for strains at or below ~0.15. Close to 0.18 strain, the momentary decrease in the gradient for Case 4 suggests some residual-stress-induced localized material yielding not observed in the experiment. Beyond the peak stress, Case 4 begins to increasingly under-predict the experimental response, and after about 0.35 strain its value is less accurate than Cases 1 and 2 (which neglect the FSI). Since this increasing under-prediction at very large strains is gradual, it is believed to be the result of either 1) lateral bulging in the simulation (which reduces the axial compressive resistance) that does not occur to the same extent in the physical experiment, or 2) less accurate modeling of the underlying rate-dependent constitutive behavior of the semi-crystalline nylon during large compressive strains of 0.3 and greater (this latter point is supported by the same reduction observation for Specimen 2 above ~0.3 strain). In addition, the compressive material constitutive relation for the extruded filament, according to its degree of crystallization, has not been quantitatively determined for this work. Note that while buckling might be postulated as the reason for reduced accuracy at the large compressive strain, buckling would not exhibit such a gradual under-prediction.

Specimen 2:

- Refering to Fig. 10a, unlike for Specimen 1, the results for Specimen 2 with Cases 1 and 2 both reveal that, without considering FSI, the predicted stress–strain response during impact may or may not resemble the experimental result, depending on whether the FFF residual stress is included. When neither FFF residual stress nor the FSI effects are present, as in Case 1, the stress under-prediction is the worst of any case over the majority of strain values (from 0 to ~0.3). Moreover, as is observed with Specimen 1, for large strains beyond ~0.3 the values of impact stress predicted by Case 1 are relatively close to the experimental values, even though the overall Case 1 trend is the worst. For Case 2, which neglects FSI (as does Case 1) but includes FFF residual stress, the overall trend predicted agrees well with the experimental results up to about 0.3 strain, suggesting that for Specimen 2 the residual stress effects are comparatively more important than the FSI effects (whereas for Specimen 1 they are both very important). Indeed, this observation seems reasonable given that Specimen 2 has greater structural rigidity due to its larger volume of the nylon and its increased number of smaller-volume fluid-filled cells.
- When FSI effects are included for Specimen 2, as in Cases 3 and 4, the predicted compressive stress–strain response may or may not resemble the trend of the experimental result, according to whether or not the FFF residual stress is included. For instance, for Case 3, which includes the FSI but neglects the FFF residual stress, the under-prediction is less severe than for Case 1 (no FFF stress, but with FSI) up to strains of about 0.3 (at which point Case 1 slightly over-predicts the impact stress). Case 4, which includes both FFF residual stress and FSI, performs best overall relative to the experimentally determined impact stress. Note that while Case 1 (without FFF stress or FSI) predicts very slightly better than Case 4 at some strain values, its prediction values and trend is worse at strains of 0.28 and greater.

4.2.2. *Comparison of experimental and numerically predicted peak compressive axial stress*

Fig. 11a and b show, respectively, the computed values of peak tensile and compressive stress components (in cylindrical coordinates) for Specimen 1 when simulating the SHPB impact test with and without inclusion of the FSI and FFF residual stress. Corresponding simulation results for Specimen 2 are shown in Fig. 11c and d. Key observations from Fig. 11a to d regarding the influence of FSI and of the residual stresses from the FFF build process on the tested specimens are noted as follows:

Specimen 1: (1) The FSI is very influential in reducing the magnitudes of all peak tensile and compressive stress components. (2) When FSI is considered, the inclusion of FFF residual stress increases the magnitudes of all peak tensile and compressive stress components. (3) When FSI is not considered, the effects of including FFF residual stress are less significant; it somewhat decreases the magnitudes of peak radial and axial stress components (tensile and compressive). Peak tensile and compressive hoop stresses increase slightly.

Specimen 2: (1) Except for the peak compressive axial stress, FSI is influential in reducing the magnitudes of all peak tensile and

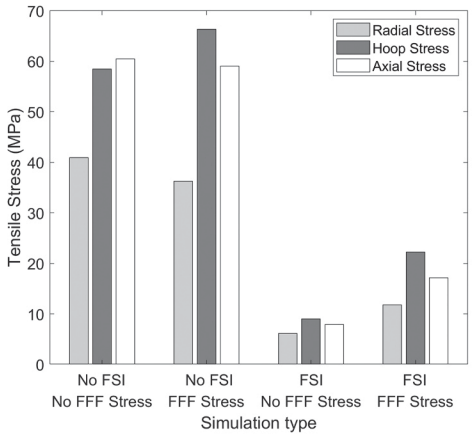

(a) Specimen 1: Peak tensile stress magnitude.

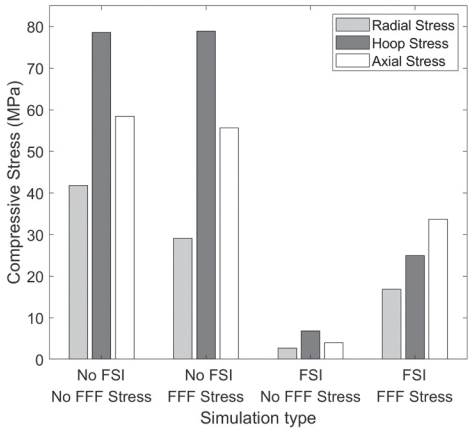

(b) Specimen 1: Peak compressive stress magnitude.

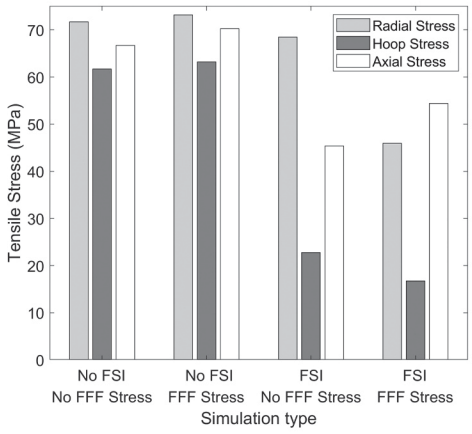

(c) Specimen 2: Peak tensile stress magnitude.

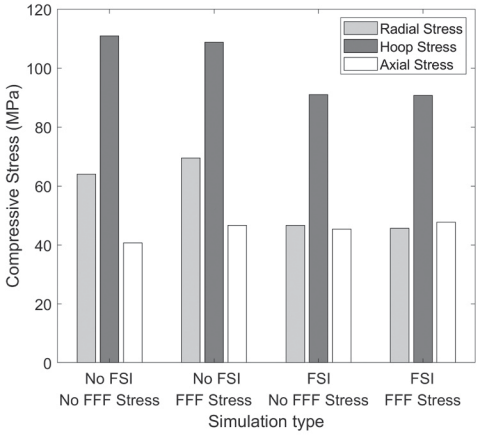

(d) Specimen 2: Peak compressive stress magnitude.

Fig. 11. Peak tensile and compressive stress components for Specimens 1 and 2 during impact simulation, with and without FSI and residual stress from FFF. Specimen 1 (5 closed-cell cavities), Specimen 2 (25 comparatively smaller closed-cell cavities). (a) Specimen 1: Peak tensile stress magnitude. (b) Specimen 1: Peak compressive stress magnitude. (c) Specimen 2: Peak tensile stress magnitude. (d) Specimen 2: Peak compressive stress magnitude.

Table 5
Comparison of experimentally determined and simulated peak compressive axial stress, with and without considering effects of FFF residual stress and FSI in numerical model.

Case number	Peak compressive axial stress, $\sigma_{Z,C}$	Specimen 1	Specimen 2
	Experiment (from Fig. 7b)	33.09 MPa[a]	48.45 MPa[b]
	[a]Mean of 5045 data points, [b]Mean of 1726 data points		
1	Simulation (w/out FFF, w/out FSI)	58.46 MPa	40.73 MPa
	Error relative to experiment (w/out FFF, w/out FSI)	76.67%	−15.93%
2	Simulation (with FFF, w/out FSI)	55.63 MPa	46.67 MPa
	Error relative to experiment (with FFF, w/out FSI)	68.11%	−3.67%
3	Simulation (w/out FFF, with FSI)	4.01 MPa	45.42 MPa
	Error relative to experiment (w/out FFF, with FSI)	−87.88%	−6.25%
4	Simulation (with FFF, with FSI)	33.73 MPa	47.80 MPa
	Error relative to experiment (with FFF, with FSI)	1.93%	−1.34%

compressive stress components. (2) Without FSI, the inclusion of FFF residual stress does not significantly change the peak tensile or compressive stress components. (3) With FSI, the inclusion of FFF residual stress decreases the peak radial and hoop tensile stresses, but increases the peak axial tensile stress.

Agreements of 1.93% and − 1.34% are indicated for the peak axial compressive stress for Specimens 1 and 2, respectively, when both FFF residual stress and FSI effects are included in the model during the impact simulation. This is observed by comparing the experimental data with Case 4 in Table 5.

When both the FSI effects and FFF residual stresses are excluded during the impact simulation, the magnitude of relative error in peak axial compressive stress for Specimen 1 increases dramatically from 1.93% to 76.67%. For Specimen 2, the relative error magnitude increases from − 1.34% to − 15.93% (as seen in Table 5 by comparing the experimental data with Case 1). As noted earlier, the FSI effect plays a much more significant role in the peak impact behavior of Specimen 1 than for Specimen 2, due to the increased rigidity of the additional polymer reinforcement structure and the corresponding reduced cavity volume in Specimen 2.

When FFF residual stresses are included (but FSI is still neglected), the relative errors for both Specimens 1 and 2 are improved, to 68.11% and − 3.67%, respectively (Case 2 in Table 5). Hence, the peak axial compressive stress is still significantly overestimated for Specimen 1 but underestimated slightly for Specimen 2.

When the FSI effects are now included, but the FFF residual stresses are excluded (Case 3), the worst prediction result arises for Specimen 1 (− 87.88%), and interestingly, the peak compressive axial stress is now significantly underestimated due to the absence of FFF residual stress. By including FSI, but neglecting the FFF stress, the Case 3 error for Specimen 2 marginally improves to − 6.25% (versus − 3.67%, when the included effects were reversed in Case 2).

An interesting insight is made by referring again to Table 2, in which the calculated peak tensile and compressive axial residual stresses from FFF, $\sigma_{Z,T}$ and $\sigma_{Z,C}$ were 7.22 MPa and 3.574 MPa, respectively, for Specimen 1. Comparing these FFF residual stresses from Table 2 to the results in Table 5 for which FFF residual stresses are neglected (76.67% error in Case 1 without FSI, and − 87.88% error in Case 3 with FSI), one can infer that the residual stress from the FFF printing induces both non-proportional and non-superposed contributions during the impact event. This circumstance is predominantly a result of the state of stress being redistributed due to the additional rigidity imposed by the entrapped air within the closed-cell cavities.

Notwithstanding the specific behavior of each specimen, the results obtained justify the physics and assumptions of the numerical modeling approach, and highlight the importance of including both residual stress from the printing process as well as FSI when assessing the impact behavior of cellular FFF builds.

5. Conclusion

This work describes simulations and experiments performed on cylindrical nylon FFF specimens manufactured with two different internal closed-cell cavity structures. Motivation for the study is to determine the influence of FFF-induced residual stresses and cellular cavity FSI on the dynamic stress response during high-speed compressive impact. Previous studies involving additively manufactured polymers have not considered residual stresses from the build process or fluid–structure coupling behavior in the dynamic response. A 2-stage numerical approach is demonstrated to simulate, respectively, the thermo-mechanical build process and the rate-dependent dynamic impact. Validation of the presented modeling framework is achieved by comparison of the bulk stress–strain response obtained with SHPB experiments. The significance of capturing both the FFF-induced residual stress and the FSI behavior when predicting the axial stress–strain response is justified by RMS stress errors within 12.77% and 11.87%, and peak stress errors within 1.93% and 1.34% for Specimens 1 and 2, respectively, when compared to the SHPB experimental results. Key findings of the study are summarized as follows:.

- Residual stress from the FFF printing process influences the dynamic behavior under high-rate impact, however its effect varies with the FFF build geometry and print pattern.
- Fluid–structure interaction effects should be considered to accurately assess the state of stress of cellular FFF builds during dynamic impact loading.
- Since the influence of FFF-induced residual stress and FSI vary significantly with the internal build geometry, a rigorous modeling technique such as the one demonstrated herein is needed to adequately predict the dynamic response for specific structures and loading conditions.

Declaration of Competing Interest

The authors declare that they have no known competing financial interests or personal relationships that could have appeared to influence the work reported in this paper.

Acknowledgement

Sunny and Malik acknowledge the support of U.S. National Science Foundation, grant no. CMMI-1762722. Chen and Lu acknowledge the support of U.S. National Science Foundation grant no. CMMI-1636306, CMMI-1661246, and CMMI-1726435. Any opinions, findings, or conclusions expressed in this paper are those of the authors and do not necessarily reflect the views of the U.S. National Science Foundation. Lu also thanks Louis A. Beecherl Chair for additional support.

References

[1] L.J. Gibson, M.F. Ashby, Cellular Solids: Structure and Properties, Cambridge University Press, 1999.
[2] N. Guo, M.C. Leu, Additive manufacturing: technology, applications and research needs, Front. Mech. Eng. 8 (2013) 215–243.
3] B. Brenken, E. Barocio, A. Favaloro, V. Kunc, R.B. Pipes, Fused filament fabrication of fiber-reinforced polymers: a review, Addit. Manuf. 21 (2018) 1–16.
[4] E.R. Denlinger, J.C. Heigel, P. Michaleris, T. Palmer, Effect of inter-layer dwell time on distortion and residual stress in additive manufacturing of titanium and nickel alloys, J. Mater. Process. Technol. 215 (2015) 123–131.
[5] S.H. Ahn, M. Montero, D. Odell, S. Roundy, P.K. Wright, Anisotropic material properties of fused deposition modeling ABS. Rapid Prototyp. J. 8 (4) (2002) 248–257.
[6] ASTM D638-14, Standard Test Method for Tensile Properties of Plastics, ASTM International, West Conshohocken, PA, 2014, www.astm.org DOI: 10.1520/D0638-14.
[7] C. Lee, S. Kim, H. Kim, S.-H. Ahn, Measurement of anisotropic compressive strength of rapid prototyping parts, J. Mater. Process. Technol. 187 (2007) 627–630.
[8] W.C. Smith, R.W. Dean, Structural characteristics of fused deposition modeling polycarbonate material, Polym. Test. 32 (8) (2013) 1306–1312.
[9] O. Es-Said, J. Foyos, R. Noorani, M. Mendelson, R. Marloth, B. Pregger, Effect of layer orientation on mechanical properties of rapid prototyped samples, Mater. Manuf. Process. 15 (1) (2000) 107–122.
[10] E. Pei, A. Lanzotti, M. Grasso, G. Staiano, M. Martorelli, The impactof process parameters on mechanical properties of parts fabricated in pla with an open-source 3-d printer, Rapid Prototyp. J. (2015).
[11] G. Alaimo, S. Marconi, L. Costato, F. Auricchio, Influence of meso-structure and chemical composition on fdm 3d-printed parts, Compos. Part B Eng. 113 (2017) 371–380.
[12] B. Tymrak, M. Kreiger, J.M. Pearce, Mechanical properties of components fabricated with open-source 3-d printers under realistic environmental conditions, Mater. Des. 58 (2014) 242–246.
[13] H.L. Tekinalp, V. Kunc, G.M. Velez-Garcia, C.E. Duty, L.J. Love, A.K. Naskar, C. A. Blue, S. Ozcan, Highly oriented carbon fiber-polymer composites via additive manufacturing, Compos. Sci. Technol. 105 (2014) 144–150.
[14] S. Guessasma, S. Belhabib, H. Nouri, Significance of pore percolation to drive anisotropic effects of 3d printed polymers revealed with x-ray μ -tomography and finite element computation, Polymer 81 (2015) 29–36.
[15] S. Guessasma, S. Belhabib, H. Nouri, O.B. Hassana, Anisotropic damage inferred to 3d printed polymers using fused deposition modelling and subject to severe compression, Eur. Polym. J. 85 (2016) 324–340.
[16] N. Mills, R. Stämpfli, F. Marone, P. Brühwiler, Finite element micromechanics model of impact compression of closed-cell polymer foams, Int. J. Solids Struct. 46 (3–4) (2009) 677–697.
[17] S.F. Sunny, G.H. Gleason, A.S. Malik, Comparison of numerical methods for fluid-structure interaction simulation of fused deposition modeled nylon components, Procedia Manuf. 34 (2019) 516–527.
[18] T. Fíla, P. Zlámal, O. Jirousek, J. Falta, P. Koudelka, D. Kyty`rˆ, T. Doktor, J. Valach, Impact testing of polymer-filled auxetics using split hopkinson pressure bar, Adv. Eng. Mater. 19 (10) (2017), 1700076.
[19] S. Ouellet, D. Cronin, M. Worswick, Compressive response of polymeric foams under quasi-static, medium and high strain rate conditions, Polym. Test. 25 (6) (2006) 731–743.
[20] H. Luo, S. Roy, H. Lu, Dynamic compressive behavior of unidirectional im7/5250-4 laminate after thermal oxidation, Compos. Sci. Technol. 72 (2) (2012) 159–166.
[21] H. Lu, P. Cary, Deformation measurements by digital image correlation: implementation of a second-order displacement gradient, Exp. Mech. 40 (4) (2000) 393–400.
[22] Y. Zhang, Characterization of the Compressive and Fracture Behavior, As Well As the Residual Tensile Strength of a Polyurethane Foam (Ph.D. thesis), Oklahoma State University, 2007.
[23] W. Chen, B. Zhang, M. Forrestal, A split hopkinson bar technique for low-impedance materials, Exp. Mech. 39 (2) (1999) 81–85.
[24] D. Karagiozova, M. Alves, On the dynamic compression of cellular materials with local structural softening, Int. J. Impact Eng. 108 (2017) 153–170.
[25] Z. Zheng, C. Wang, J. Yu, S.R. Reid, J.J. Harrigan, Dynamic stress-strain states for metal foams using a 3d cellular model, J. Mech. Phys. Solids 72 (2014) 93–114.
[26] Z. Wang, Y. Zhou, P. Mallick, Effects of temperature and strain rate on the tensile behavior of short fiber reinforced polyamide-6, Polym. Compos. 23 (5) (2002) 858–871.
[27] B. Brenken, E. Barocio, A. Favaloro, V. Kunc, R.B. Pipes, Development and validation of extrusion deposition additive manufacturing process simulations, Addit. Manuf. 25 (2019) 218–226.
[28] C.N. Velisaris, J.C. Seferis, Crystallization kinetics of polyetheretherketone (peek) matrices, Polym. Eng. Sci. 26 (1986) 1574–1581.
[29] B. Brenken, Extrusion Deposition Additive Manufacturing of Fiber Reinforced Semi-Crystalline Polymers (Ph.D. thesis), Purdue University, 2017.
[30] A. Cattenone, S. Morganti, G. Alaimo, F. Auricchio, Finite element analysis of additive manufacturing based on fused deposition modeling: distortions prediction and comparison with experimental data, J. Manuf. Sci. Eng. 141 (2019).
[31] G. Madireddy, C. Li, J. Liu, M.P. Sealy, Modeling thermal and mechanical cancellation of residual stress from hybrid additive manufacturing by laser peening, Nanotechnol. Precis. Eng. 2 (2) (2019) 49–60.
[32] A. D'Amico, A.M. Peterson, An adaptable fea simulation of material extrusion additive manufacturing heat transfer in 3d, Addit. Manuf. 21 (2018) 422–430.
[33] T. D'Amico, A.M. Peterson, Bead parameterization of desktop and room-scale material extrusion additive manufacturing: how print speed and thermal properties affect heat transfer, Addit. Manuf. (2020), 101239.
[34] M. Roy, R. Yavari, C. Zhou, O. Wodo, P. Rao, Prediction and experimental validation of part thermal history in the fused filament fabrication additive manufacturing process, J. Manuf. Sci. Eng. 141 (2019).
[35] J. Heigel, P. Michaleris, E.W. Reutzel, Thermo-mechanical model development and validation of directed energy deposition additive manufacturing of ti-6al-4v, Addit. Manuf. 5 (2015) 9–19.
[36] P. Peyre, P. Aubry, R. Fabbro, R. Neveu, A. Longuet, Analytical and numerical modelling of the direct metal deposition laser process, J. Phys. D Appl. Phys. 41 (2008), 025403.
[37] V. Neela, A. De, Three-dimensional heat transfer analysis of lens tm process using finite element method, Int. J. Adv. Manuf. Technol. 45 (9–10) (2009) 935.
[38] M. Chiumenti, M. Cervera, A. Salmi, C.A. De Saracibar, N. Dialami, K. Matsui, Finite element modeling of multi-pass welding and shaped metal deposition processes, Comput. Methods Appl. Mech. Eng. 199 (37–40) (2010) 2343–2359.
[39] V. Manvatkar, A. Gokhale, G.J. Reddy, A. Venkataramana, A. De,, Estimation of melt pool dimensions, thermal cycle, and hardness distribution in the laser-engineered net shaping process of austenitic stainless steel, Metall. Mater. Trans. A 42 (13) (2011) 4080–4087.
[40] E.R. Denlinger, J.C. Heigel, P. Michaleris, Residual stress and distortion modeling of electron beam direct manufacturing ti-6al-4v, Proc. Inst. Mech. Eng. Part B J. Eng. Manuf. 229 (2015) 1803–1813.
[41] S. Srivastava, R.K. Garg, V.S. Sharma, N.G. Alba-Baena, A. Sachdeva, R. Chand, S. Singh, Multi-physics continuum modelling approaches for metal powder additive manufacturing: a review, Rapid Prototyp. J. (2020).
[42] E.R. Denlinger, P. Michaleris, Effect of stress relaxation on distortion in additive manufacturing process modeling, Addit. Manuf. 12 (2016) 51–59.
[43] W.M. Kays, Convective Heat and Mass Transfer, Tata McGraw-Hill Education, 2012.
[44] M.F. Gouge, J.C. Heigel, P. Michaleris, T.A. Palmer, Modeling forced convection in the thermal simulation of laser cladding processes, Int. J. Adv. Manuf. Technol. 79 (1–4) (2015) 307–320.
[45] S.W. Churchill, H.H. Chu, Correlating equations for laminar and turbulent free convection from a vertical plate, Int. J. Heat. Mass Transf. 18 (11) (1975) 1323–1329.
[46] W.M. Lai, D.H. Rubin, E. Krempl, D. Rubin, Introduction to Continuum Mechanics, Butterworth-Heinemann, 2009.
[47] N.E. Dowling, Mechanical Behavior of Materials: Engineering Methods for Deformation, Fracture, and Fatigue, Pearson, 2012.
[48] M.H. Sadd, Elasticity: Theory, Applications, and Numerics, Academic Press, 2009.
[49] H. Xia, J. Lu, G. Tryggvason, A numerical study of the effect of viscoelastic stresses in fused filament fabrication, Comput. Methods Appl. Mech. Eng. 346 (2019) 242–259.
[50] M.F. Tomé, A. Castelo, A.M. Afonso, M.A. Alves, F.T. d. Pinho, Application of the log-conformation tensor to three-dimensional time-dependent free surface flows, J. Non-Newton. Fluid Mech. 175 (2012) 44–54.
[51] R.I. Tanner, A theory of die-swell revisited, J. Non-Newton. Fluid Mech. 129 (2) (2005) 85–87.
[52] Callister W. D., Rethwisch D., Materials Science and Engineering, an Introduction, John Wiley & Sons, Inc., 2013.
[53] P. Michaleris, Modeling metal deposition in heat transfer analyses of additive manufacturing processes, Finite Elem. Anal. Des. 86 (2014) 51–60.
[54] L.-E. Lindgren, A. Lundbäck, M. Fisk, R. Pederson, J. Andersson, Simulation of additive manufacturing using coupled constitutive and microstructure models, Addit. Manuf. 12 (2016) 144–158.
[55] M. Panasiti, E.W. Lemmon, S. Penoncello, R. Jacobsen, D.G. Friend, Thermodynamic properties of air from 60 to 2000 k at pressures up to 2000 mpa, Int. J. Thermophys. 20 (1999) 217–228.
[56] P. Morse, K. Ingard, Theoretical Acoustics, Mcgraw-Hill, New York, 1968, pp. 467–553, reprinted.
[57] L.D. Landau, E.M. Lifshitz, Course of Theoretical Physics, Elsevier, 2013.
[58] G. Batchlor, An Introduction to Fluid Dynamics, Cambridge University Press, London, 1967, p. 550.
[59] R.A. Gingold, J.J. Monaghan, Smoothed particle hydrodynamics: theory and application to non-spherical stars, Mon. Not. R. Astron. Soc. 181 (3) (1977) 375–389.
[60] P.W. Cleary, Modelling confined multi-material heat and mass flows using sph, Appl. Math. Model. 22 (1998) 981–993.

[61] J.J. Monaghan, Smoothed particle hydrodynamics, Annu. Rev. Astron. Astrophys. 30 (1) (1992) 543–574.
[62] P.W. Cleary, J.J. Monaghan, Conduction modelling using smoothed particle hydrodynamics, J. Comput. Phys. 148 (1) (1999) 227–264.
[63] R. Gingold, J. Monaghan, Kernel estimates as a basis for general particle methods in hydrodynamics, J. Comput. Phys. 46 (3) (1982) 429–453.
[64] G.R. Johnson, R.A. Stryk, S.R. Beissel, Sph for high velocity impact computations, Comput. Methods Appl. Mech. Eng. 139 (1–4) (1996) 347–373.
[65] H. Wendland, Piecewise polynomial, positive definite and compactly supported radial functions of minimal degree, Adv. Comput. Math. 4 (1) (1995) 389–396.
[66] J.J. Monaghan, J.C. Lattanzio, A refined particle method for astrophysical problems, Astron. Astrophys. 149 (1985) 135–143.
[67] K. Chou, Y. Zhang, A parametric study of part distortion in fused deposition modeling using three dimensional element analysis, J. Eng. Manuf. 222 (2008) 959–967.
[68] J. Kosmann, O. Völkerink, M. Schollerer, D. Holzhüter, C. Hühne, Digital image correlation strain measurement of thick adherend shear test specimen joined with an epoxy film adhesive, Int. J. Adhes. Adhes. 90 (2019) 32–37.
[69] J.E. Seppala, K.D. Migler, Infrared thermography of welding zones produced by polymer extrusion additive manufacturing, Addit. Manuf. 12 (2016) 71–76.